Structure-performance relationships of four lysosomal markers used for the imaging of HT-29 cancer cells and a cellular model of lysosomal storage disease (Niemann-Pick C)

Diego Navarro-Barreda [a], Begoña Bedrina [a], César A. Angulo-Pachón [a], Juan F. Miravet [a], Dolores Pérez-Sala [b], Francisco Galindo [a,*]

[a] *Departamento de Química Inorgánica y Orgánica, Universitat Jaume I, Avda. Sos Baynat s/n, 12071, Castelló de la Plana, Spain*
[b] *Departamento de Biología Estructural y Química, Centro de Investigaciones Biológicas Margarita Salas (CSIC), Ramiro de Maeztu, 9, 28040, Madrid, Spain*

ARTICLE INFO

ABSTRACT

Four new BODIPY derivatives with a potential tendency to aggregation have been synthesized and characterized by means of NMR techniques, mass spectrometry and UV–Vis/fluorescence spectroscopies. The objective of this study is to determine which structural factors of the new molecules influence most notably the cellular uptake, intracellular location and fluorescence imaging abilities. The behaviour of the compounds in organic solvent and aqueous solution has been studied. In organic solvents (DMSO, ethanol and toluene), the photophysical properties of the new molecules are almost independent of the building blocks used to synthesize the pendant moieties (non-fluorogenic parts). In an aqueous environment (HEPES Buffer Solution, pH 7), at 10 μM, three of the compounds (**1**, **2** and **4**) tend to form weakly emissive nanoparticles (DLS determination) whereas one of them (**3**) remains soluble and highly fluorescent. In the nanomolar range of concentration, all the compounds are aqueous soluble. The cellular internalisation of the compounds (10 nM) has been studied in human colon adenocarcinoma HT-29 cells by means of flow cytometry and confocal laser scanning microscopy. All the compounds were uptaken by HT-29 cells, but notably molecule **3** (made with lysine as a building block) was the one displaying a higher loading and a more clear lysosomal location (0.88 Pearson's correlation coefficient in colocalization assays using lysosomal fluorescent probe LysoTracker DND-99). Molecule **3** also performed better than the valine derivative **1** as a lysosomal marker in a cellular model (human adrenal carcinoma SW13/cl.2 cells) of lysosomal storage disease (Niemann-Pick type C).

1. Introduction

Lysosomes are acidic organelles responsible for vital functions in living cells, such as degradation of waste products or defensive action against pathogenic microorganisms [1]. Inadequate functioning of these organelles is associated with common pathologies such as cancer [2] and Alzheimer's disease [3]. Consequently, the proper knowledge of their internal biochemistry is important to design drugs to treat such disorders. In a different context, the endo-lysosomal pathway constitutes the entrance door for viral pathogens like influenza virus, West Nile virus and others. Thus, antiviral drugs like chloroquine and hydroxychloroquine and other lysosomotropic drugs work increasing the pH of these organelles and hence hindering the entrance of some viral pathogens [4]. More recently, the lysosome has been the centre of the debate

regarding potential therapeutic approaches to fight SARS-CoV-2 [5]. In another realm, one group of specific diseases linked to lysosomes, known as lysosomal storage disorders, involves the accumulation of intracellular waste products in these organelles [6,7]. An example is the Niemann-Pick type C disease [8] which is characterized by the accumulation of cholesterol inside lysosomes.

Fluorescence probes targeting the lysosome have been the key to understanding its functions, and a vast number of molecules have been designed, synthesized and tested in living cells, allowing much of the current knowledge on this cellular structure. The variety of fluorophores used in the design of such intracellular reporters is overwhelming: xanthenes [9,10], BODIPYs [11–13], naphthalimides [13,14] and others [15–25]. Recently, a series of reviews have been published dealing with probes targeted to specific organelles [26,27]. The great part of the

publications described so far report the fine tuning of well-known fluorophores such as those mentioned above, introducing substituents of diverse nature, length, and branching that affect directly their photophysical properties like absorption or emission wavelengths, fluorescence quantum yields or lifetimes, photostability, etc. Sometimes, combinations of two fluorophores give rise to interesting intramolecular phenomena such as energy or electron transfer processes. Less attention has been paid to the part of the molecule not strictly participating in the emissive event, normally having a secondary role in modulating properties such as membrane translocation ability or resistance to enzyme degradation or to photobleaching. For instance, Urano et al. studied the structure-property relationships of four BODIPY dyes, which differ only in the substitution of the peripheral aniline bearing different combinations of methyl, ethyl and hydrogen substituents at the nitrogen, finding notable differences in the performance of such probes as lysosomal imaging molecules in bovine pulmonary artery endothelial cells [28]. In another example, Rong et al. studied the lysosomal imaging capabilities in HeLa cells of a series of bis-naphthalimide derivatives differing only in the substitution at the terminal end of the dyads (including subtle changes such as the number of methylenes in a pendant group) [14]. In a more dramatic case, Zhou et al. reported two seemingly identical phosphinate xanthenic derivatives differing only in the substitution of the peripheral nitrogen atoms (methyl *vs.* fused cycloalkyl) which locate intracellularly in HeLa cells in a very different manner (lysosome *vs.* mitochondria, respectively) [18]. But less attention has been paid to relationships between the tendency to aggregation and the imaging performance in the cellular milieu.

Here we describe the synthesis and characterization of four molecules (**1–4**, Fig. 1) bearing the same BODIPY emitting core but differing in the pendant chain accompanying the fluorophore. Their ability as fluorescent cell markers has been evaluated using confocal microscopy and flow cytometry as bioanalytical tools. Significant differences have been found in the uptake of the studied compounds, which reinforces the idea that the non-emissive part of the probe is as important as the fluorogenic core to achieve proper cellular internalisation and fluorescence imaging. One of the compounds (**3**), with a low tendency to form aggregates in an aqueous environment, has been especially effective for

the fluorescence staining of lysosomes of a human colorectal adenocarcinoma cell line (HT-29). In addition to this cellular type, the ability of this compound for imaging has been confirmed in a pharmacological cellular model of Niemann-Pick type C disease, showing an excellent internalisation and lysosomal staining, reflecting the impact of the disorder.

Much effort has been put to answer the question of which architectural motif is best suited for the targeting of a certain fluorophore towards a specific organelle [29–31]. However, the theoretical answers, although valuable, do not take into account apparently secondary phenomena like self-assembly into nanostructures. The present research advocates for the experimental assay of batteries of compounds showing chemical diversity, including molecules displaying a marked tendency to aggregation.

2. Experimental section

2.1. Materials and instrument

Commercially available reagents and *HPLC* grade solvents were purchased from commercial suppliers and used without further purification. Reactions that required an inert atmosphere were carried out under a nitrogen atmosphere. NMR spectra were recorded on an Agilent VNMR System spectrometer (500 MHz for ^{1}H NMR, 125 MHz for ^{13}C NMR) or Bruker Advance III HD spectrometers (400 MHz and 300 MHz for ^{1}H NMR, 101 MHz and 75 MHz for ^{13}C NMR) in the indicated solvent at 30 °C. All chemical shifts (δ) are quoted in parts per million (ppm) downfield from tetramethylsilane (TMS) and coupling constants (J) are quoted in Hertz (Hz). Mass spectra were recorded at Mass Spectrometry triple Quadrupole Q-TOF Premier (Waters) with simultaneous Electrospray and APCI Probe. The photophysical properties were measured with a JASCO FP-8300 fluorometer and a JASCO V-630 UV–Vis spectrophotometer. Lifetime measurements were recorded using the time-correlated single-photon counting (TCSPC) technique. The excitation source was a nanoLED of 464 nm (1.4 ns pulse width) and the fitting analysis was done using the software provided by IBH. All dynamic light scattering (DLS) measurements were recorded using a Zetasizer Nano ZS
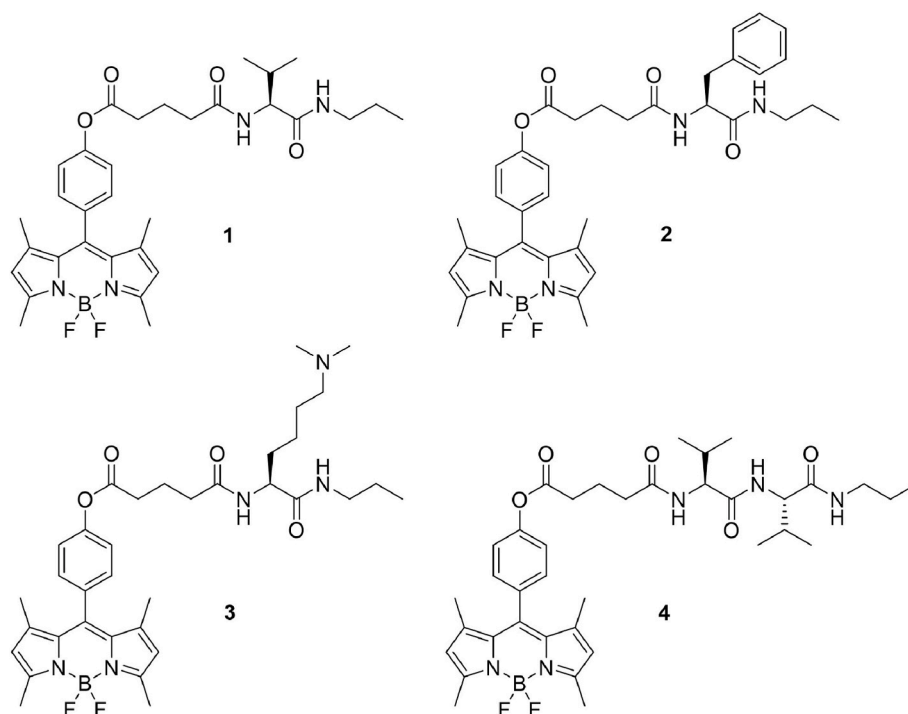

Fig. 1. Synthetic BODIPY probes with amino acid residues **1–4**.

(Malvern Instruments, UK). Automatic optimization of beam focusing and attenuation was applied for each sample.

2.2. Synthesis

2.2.1. Synthesis of 1 - 4

To a stirred solution of B (see Supplementary data) (0.22 mmol, 1.0 eq.) in $CHCl_3$ (50 mL) at room temperature, DIPEA (*N,N*-diisopropyl-*N*-ethylamine, 0.24 mmol, 1.1 eq.) and TBTU (*O*-(Benzotriazol-1-yl)-*N,N*, *N′,N′*,-tetramethyluronium tetrafluoroborate, 0.24 mmol, 1.1 eq.) were added, and the mixture is stirred for 25 min. Then, the appropriate *N*-unprotected amino acid (0.22 mmol, 1.0 eq.) was added and the reaction mixture was stirred overnight. After that, the reaction mixture was evaporated to dryness under reduced pressure. The residue was dissolved in $CHCl_3$ (50 mL) and washed twice with 1.0 M HCl (30 mL), twice with saturated $NaHCO_3$ (30 mL) and once with brine (30 mL). The organic phase is dried over Na_2SO_4 and evaporated under reduced pressure. The solid obtained is washed with petroleum ether and dried to afford **1–4**.

4-(5,5-difluoro-1,3,7,9-tetramethyl-5H-4λ4,5λ4-dipyrrolo[1,2-c:2′,1′-f] [1–3]diazaborinin-10-yl)phenyl (S)-5-((3-methyl-1-oxo-1-(propylamino)butan-2-yl)amino)-5-oxopentanoate *(1)*. Yield: 73%; ^{1}H NMR (300 MHz, $CDCl_3$, δ): 7.35–7.28 (m, 2H), 7.26–7.19 (m, 2H), 6.18 (d, *J* = 8.5 Hz, 1H), 5.99 (s, 2H), 5.85 (s, 1H), 4.18 (dd, *J* = 8.7, 7.1 Hz, 1H), 3.36–3.09 (m, 2H), 2.67 (t, *J* = 7.2 Hz, 2H), 2.55 (s, 6H), 2.40 (t, *J* = 7.0 Hz, 2H), 2.14–2.02 (m, 3H), 1.56–1.47 (m, 2H), 1.42 (s, 6H), 1.03–0.85 (m, 9H); ^{13}C NMR (101 MHz, $CDCl_3$, δ): 172.1, 171.4, 171.2, 155.9, 151.4, 143.3, 140.8, 132.6, 131.6, 129.4, 122.6, 121.5, 58.9, 41.4, 35.3, 33.5, 31.3, 22.9, 20.8, 19.4, 18.5, 14.7, 11.5; HRMS (ESI) *m/z*: $[M+H]^+$ calcd for $C_{32}H_{41}BF_2N_4O_4$ 594.3309; found, 594.3304.

4-(5,5-difluoro-1,3,7,9-tetramethyl-5H-4λ4,5λ4-dipyrrolo[1,2-c:2′,1′-f] [1–3]diazaborinin-10-yl)phenyl (S)-5-oxo-5-((1-oxo-3-phenyl-1-(propylamino)propan-2-yl)amino)pentanoate *(2)*. Yield: 51%; ^{1}H NMR (400 MHz, $CDCl_3$, δ): 7.42–7.15 (m, 9H), 6.29 (d, *J* = 7.5 Hz, 1H), 5.99 (s, 2H), 5.52 (t, *J* = 4.9 Hz, 1H), 4.71–4.36 (m, 1H), 3.23–2.90 (m, 4H), 2.70–2.46 (m, 8H), 2.35 (t, *J* = 7.2 Hz, 2H), 2.19–1.97 (m, 2H), 1.50–1.17 (m, 8H), 0.78 (t, *J* = 7.4 Hz, 3H); ^{13}C NMR (101 MHz, $CDCl_3$, δ): 171.8, 171.4, 170.7, 155.9, 151.3, 143.3, 140.8, 136.9, 132.6, 131.6, 129.4, 128.9, 127.2, 122.6, 121.5, 55.0, 41.4, 39.1, 35.2, 33.4, 22.7, 20.6, 14.7, 11.4; HRMS (ESI) *m/z*: $[M+Na]^+$ calcd for $C_{36}H_{41}BF_2N_4O_4$ 664.3123; found, 664.3121.

4-(5,5-difluoro-1,3,7,9-tetramethyl-5H-4 λ4,5 λ4-dipyrrolo[1,2-c:2′,1′-f] [1–3]diazaborinin-10-yl)phenyl 5-((6-(dimethylamino)-1-oxo-1-(propylamino)hexan-2-yl)amino)-5-oxopentanoate *(3)*. Yield: 26%; ^{1}H NMR (400 MHz, $CDCl_3$, δ): 7.50 (d, *J* = 7.3 Hz, 1H), 7.33–7.25 (m, 4H), 7.05 (t, *J* = 5.5 Hz, 1H), 5.98 (s, 2H), 4.48 (dd, *J* = 13.8, 7.1 Hz, 1H), 3.25–3.08 (m, 3H), 3.04–2.93 (m, 1H), 2.84 (d, *J* = 4.9 Hz, 3H), 2.80 (d, *J* = 4.9 Hz, 3H), 2.68 (t, *J* = 7.4 Hz, 2H), 2.55 (s, 6H), 2.51 (t, *J* = 7.3 Hz, 2H), 2.22–2.03 (m, 2H), 1.99–1.81 (m, 5H), 1.79–1.66 (m, 1H), 1.57–1.49 (m, 2H), 1.42 (s, *J* = 7.1 Hz, 6H), 0.90 (t, *J* = 7.4 Hz, 3H); ^{13}C NMR (101 MHz, $CDCl_3$, δ): 173.2, 171.7, 171.5, 155.8, 151.4, 143.3, 140.9, 132.5, 131.6, 129.3, 122.7, 121.5, 56.9, 53.1, 43.7, 42.8, 41.4, 35.1, 33.7, 31.1, 30.6, 23.9, 22.8, 21.9, 20.9, 14.7, 11.6; HRMS (ESI) *m/z*: $[M+H]^+$ calcd for $C_{35}H_{48}BF_2N_5O_4$ 651.3883; found, 651.3881.

4-(5,5-difluoro-1,3,7,9-tetramethyl-5H-4λ4,5λ4-dipyrrolo[1,2-c:2′,1′-f] [1–3]diazaborinin-10-yl)phenyl 5-(((S)-3-methyl-1-(((S)-3-methyl-1-oxo-1-(propylamino)butan-2-yl)amino)-1-oxobutan-2-yl) amino)-5-oxopentanoate *(4)*. Yield: 64%; ^{1}H NMR (300 MHz, MeOD, δ): 7.44–7.27 (m, 4H), 6.08 (s, *J* = 10.3 Hz, 2H), 4.28–4.04 (m, 2H), 3.22–3.04 (m, 2H), 2.68 (t, *J* = 7.5 Hz, 2H), 2.57–2.36 (m, 8H), 2.13–1.95 (m, 4H), 1.61–1.39 (m, 8H), 1.07–0.76 (m, 15H); HRMS (ESI) *m/z*: $[M+Na]^+$ calcd for $C_{37}H_{50}BF_2N_5O_5$ 715.3807; found, 715.3815. Due to its limited solubility, the ^{13}C NMR spectrum could not be recorded.

2.3. Cells and treatments

Human colon adenocarcinoma HT-29 cells were from the American Type Culture Collection and were cultured in FluoroBrite™ DMEM (Gibco™ A1896701, Thermo Fisher Scientific). SW13/cl.2 were the generous gift from Dr A. Sarriá (University of Zaragoza, Spain) [32], and were cultured as previously described [33]. For pharmacological induction of the Niemann-Pick phenotype [34], cells were cultured for 24 h in the presence of 10 μM U18666A or vehicle (0.1% (v/v) DMSO), as previously described [35], before incubation with the lysosomal probes **1** and **3**.

2.4. Fluorescence microscopy

HT-29 cells (grown to 50–60% confluence) in a sterilized Ibidi® μ-Slide (4 well glass bottom) were preincubated with **1–4** (10 nM) for 20 min at 37 °C, followed by incubation with LysoTracker DND-99 (100 nM, a commercial lysosomal indicator) for 30 min at 37 °C. After washing with PBS, cells were kept in FluoroBrite DMEM medium and visualized under the confocal microscope. Cells were imaged live on an inverted confocal microscope Leica TCS SP8. Images were obtained with an HC PL APO CS2 63 × /1.40 oil immersion objective. The **1–4** excitation wavelengths and the LysoTracker DND-99 were set at 488 nm and 561 nm, respectively. The fluorescent emissions wavelength was recorded from 500 to 550 nm for **1–4** and from 620 to 680 nm for LysoTracker DND-99. For colocalization analysis, the fluorescence intensity profiles were traced along an arbitrary line using LasX software (Leica Microsystems); the Pearson's correlation coefficients were calculated from the whole image using the Coloc2 plugin in ImageJ.

Incubation of SW13/cl.2 cells with lysosomal probes was carried out as above. Cells were imaged live on a Leica AF6000 LX with excitation and emission wavelengths at 488 and 563, respectively. Subsequently, cells were fixed with 4% (w/v) paraformaldehyde and observed in a Leica SP8 confocal microscope. Images were acquired every 0.5 μm and overall projections are shown.

2.5. Flow cytometry assay

HT-29 cells in a 6-/12-well plate (grown to 70–80% confluence) were incubated with **1–4** (10 nM) for 20 min at 37 °C. Cells were washed with PBS (1.5 mL/well) twice and detached from the culture dishes by incubation with 0.25% trypsin + EDTA. After centrifugation at 5000 rpm for 5 min, cells were washed again with PBS to remove away any dye excess. Cells were re-suspended in PBS (1 mL) and analyzed on a BD Accuri™ C6 flow cytometer. After exclusion of the cellular debris by appropriate gating on the SSC versus FSC plots, fluorescence intensity was analyzed on channel FL-1 (excitation at 488 nm; emission collected at 533/30 nm) measuring at least 20,000 cells for each sample. The results are reported as the mean fluorescence intensity from the flow cytometry histograms comparing with the blank group (unstained cells).

3. Results and discussion

The structures of **1–4** were designed following the model of analogous architectures described by us in the past. The combination of amino acid moieties and long alkyl chains has led to compounds with marked self-assembling properties [36–38]. This study aims to determine which structural factors of the pendant chain influence most notably the cellular uptake, intracellular location and fluorescence imaging performance. The synthesis of **1–4**, bearing a BODIPY fluorophore and amino acid-derived chains, was carried out following a convergent route, as illustrated in the Electronic Supporting Information (ESI) file. All the compounds were chemically characterized by means of mono- and bi-dimensional NMR techniques and mass spectrometry. Before the biological assays, the photophysical features of all the compounds were determined. The absorption and emission spectra of all the compounds

are very similar in organic solvents such as DMSO, ethanol and toluene (Fig. 2A). Table 1 shows the complete photophysical data of all molecules, including emission quantum yields, fluorescence lifetimes and radiative (k_r) and non-radiative (k_{nr}) decay constants.

The position of the absorption and emission maxima of the spectra of **1–4** does not change notably with solvent polarity nor depends on the pendant chain of the compound. The emission quantum yields (φ_F) of **1–4** in organic solvents lie within the range 0.50–0.63 and the mono-exponential fluorescence lifetimes (τ_F) recorded are from 3.2 to 3.8 ns (Figs. S1 and S2). All the described values are similar to the parameters described in organic solvents for other BODIPY tagged molecules described in the literature [39]. For instance, the group of Resch-Genger has described comprehensive families of BODIPY dyes displaying values of φ_F in the range of 0.5–0.9 and τ_F of about 3–6 ns both in polar solvents [40,41]. Calculated radiative and non-radiative decay constants for **1–4** are also in the range of reported values in the literature [40,41] (k_r = 0.13–0.19 ns^{-1} and k_{nr} = 0.11–0.14 ns^{-1}), irrespective of the solvent and the chemical structure of the probe. The independency of φ_F and τ_F on the architecture of the studied molecules implies that the fluorogenic structure and the rest of the molecule behave almost independently in organic solvents. A potential photoinduced electron transfer (PET) process between the dimethylamino group and the bodipy photoactive part in **3** is also absent, according to the invariant values of φ_F and τ_F presented by **3** in comparison to the other systems under consideration.

In contrast, in an aqueous solution (0.1 M HEPES, pH 7.00), the spectral features of **1–4**, at a concentration of 10 μM, depend largely on the nature of the architecture of the pendant moiety. The absorption spectra of **1, 2** and **4** are clearly broadened, whereas that of **3** remains sharp (Fig. 2B). This type of spectral feature has been described frequently for BODIPY derivatives showing aggregation [42]. Specific

Table 1
Overview of the photophysical properties of the synthesized BODIPY dyes measured in different solvents.

	Solvent	λ_{abs} (log ε) [nm]	λ_{em} [nm]	φ_F[a]	τ_F [ns][b]	k_r [ns^{-1}][c]	k_{nr} [ns^{-1}][c]
1	DMSO	502 (4.84)	515	ND	ND	ND	ND
	Ethanol	500 (4.86)	509	0.54	3.5	0.15	0.13
	Toluene	504 (4.89)	515	0.58	3.3	0.18	0.13
	H$_2$O[d]	502	509	ND	ND	ND	ND
2	DMSO	502 (4.83)	515	ND	ND	ND	ND
	Ethanol	500 (4.84)	509	0.57	3.4	0.17	0.13
	Toluene	504 (4.85)	515	0.63	3.3	0.19	0.11
	H$_2$O[d]	528	507	ND	ND	ND	ND
3	DMSO	502 (4.80)	513	ND	ND	ND	ND
	Ethanol	500 (4.79)	509	0.53	3.3	0.16	0.14
	Toluene	504 (4.80)	515	0.55	3.2	0.17	0.14
	H$_2$O[d]	498 (4.70)	510	0.50	3.8	0.13	0.13
4	DMSO	502 (4.67)	514	ND	ND	ND	ND
	Ethanol	500 (4.68)	509	0.57	3.4	0.17	0.13
	Toluene	504 (4.71)	514	0.62	3.3	0.19	0.12
	H$_2$O[d]	501	508	ND	ND	ND	ND

Abbreviation: ND; not determined.
[a] Using fluorescein as a standard in 0.1 M NaOH solution (φ_F = 0.91, λ_{ex} = 470 nm).
[b] Mono exponential fit.
[c] $k_r = \varphi_F/\tau_F$ and $k_{nr} = (1 - \varphi_F)/\tau_F$.
[d] 0.1 M HEPES buffered solution, pH 7.00 (reliable fluorescence measurements only possible for **3** since **1, 2** and **4** form aggregates).

differences can be found between phenylalanine derivative **2** and valine derivatives **1** and **4** since the former displays an absorption band clearly red-shifted (maximum at 528 nm) relative to the positions of the bands of **1** and **4** (maxima at 502 and 501 nm, respectively). The group of
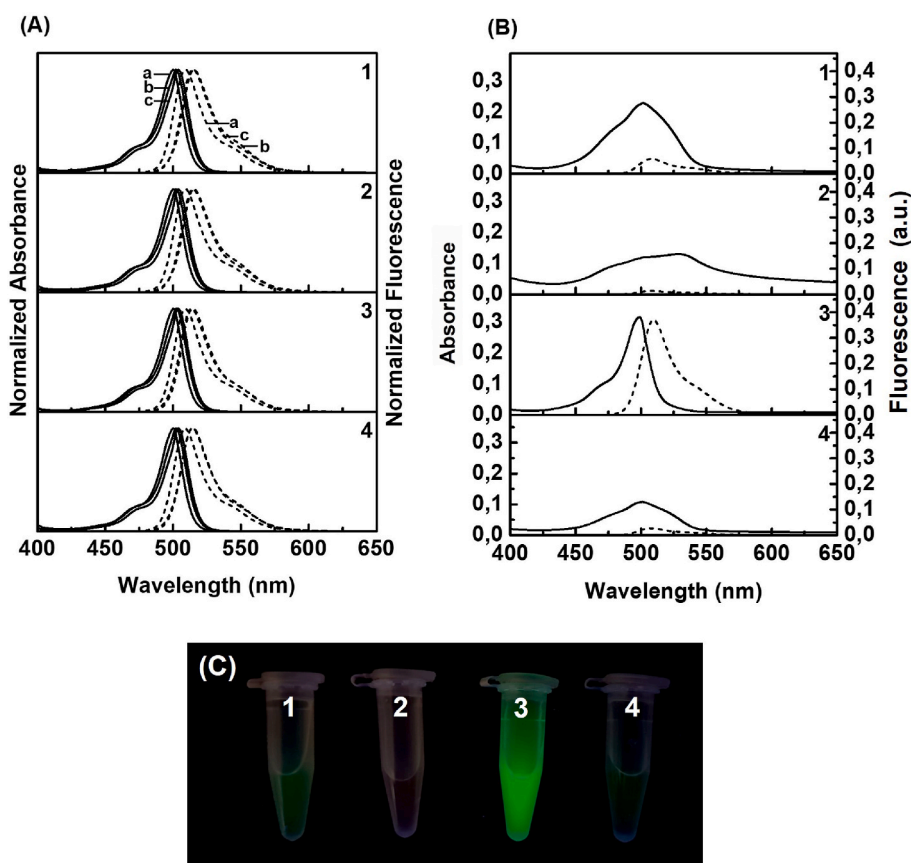

Fig. 2. A: Normalized absorption (solid line) and emission spectra (dashed line, λ_{ex} = 475 nm) of **1–4** (10 μM) in (a) ethanol, (b) DMSO and (c) toluene; B: Absorption (solid line) and emission (dashed line, λ_{ex} = 475 nm) of **1–4** in aqueous solution (0.1 M HEPES buffer, pH 7.00); C: Photograph of aqueous solutions of **1–4** under UV excitation (365 nm).

Johansson has studied in detail the formation of ground state dimers of BODIPY derivatives and has suggested two types of ensembles [43]: D_I-type dimers (fluorophores stacked) with absorptions around 447 nm, hence below the maximum of the monomeric form (ca. 500 nm) and D_{II}-type dimers (fluorophores in the same plane) with absorptions around 580 nm. None of the dimeric forms can be observed in the case of **3**, thus it can be assumed that it remains solvated in an aqueous solution. Regarding the fluorescence properties, the dimethyllysine derivative **3** remains highly emissive in aqueous solution (neutral pH), with $\varphi_F = 0.50$ and $\tau_F = 3.8$ ns, whereas the emissive properties of **1**, **2** and **4** can be hardly measured (estimated $\varphi_F < 0.05$). Visually, emission performance differences between the described molecules can be seen in Fig. 2C. The stability of solutions of **1–4** (0.1 M HEPES, pH 7.00) overtime was also checked, as can be seen in Fig. S3.

The formation of nanostructures at a concentration of 10 μM is supported by Dynamic Light Scattering (DLS) measurements (see Fig. S6). Whereas samples of **1**, **2** and **4** in 0.1 M HEPES, pH 7.00 yielded clearly signal dispersion compatible with nanoparticles of ca. 100 nm, molecule **3** afforded only some background noise, which is compatible with the complete solubilisation of this probe. Notably, among the self-associating molecules **1**, **2** and **4**, the one showing the highest derived count rate in DLS was phenylalanine derivative **2**. It must be recalled that this species is also the one displaying the most distorted absorption spectrum as can be seen in Fig. 2B. In the normalized fluorescence spectra of **1–4**, it can also be appreciated a different behaviour between soluble 3 and aggregated **1**, **2** and **4** (shoulder at 530–540 nm) (Fig. S4, left). At a much lower concentration (10 nM) of **1–4**, the optical properties of all the molecules are similar, which points to complete solubilisation of them (Fig. S4, right). Despite the ability of **3** to remain in solution at 10 μM, when the concentration is increased to 100 μM the formation of aggregates is also evident from the fluorescence spectrum (Fig. S5). To summarize, at a very low concentration (10 nM) all the compounds remain soluble in aqueous solution, at an intermediate concentration (10 μM) **1**, **2** and **4** form nanoparticles whereas **3** remains soluble, and at a very high concentration (100 μM) all the molecules form aggregates.

The ability of **1–4** to be incorporated intracellularly was tested using human colon adenocarcinoma HT-29 cells by flow cytometry as a bioanalytical technique. Solutions of **1–4** at 10 nM were incubated with HT-29 cells for 20 min at 37 °C. After this time, the fluorescence of samples was measured and it became clear that **1** and **3** were the compounds marking the cells with higher intensity, especially **3**, which provides a
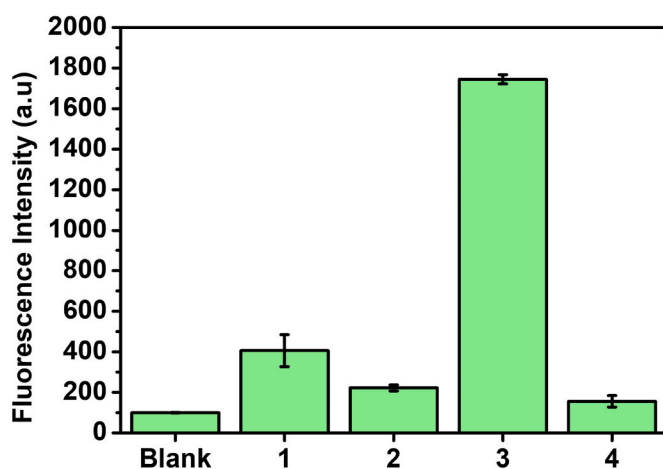

Fig. 3. Analysis by flow cytometry of samples of HT-29 cells incubated with **1–4**. The bar graph shows the mean of fluorescence intensities of selected areas within the scatter plot, which are representative of the uptake of the probes into the cells (see Fig. S7, ESI). All values are presented as the mean ± standard, compared with the blank group (no probe added).

signal about 8-fold more intense than the average of the other molecules (Fig. 3).

Next, **1–4** were studied in more detail and used to image HT-29 cells using confocal laser scanning microscopy (CLSM). As it can be observed in Fig. 4, all the compounds internalized in the cells but with notable differences. Molecule **3** accumulates giving higher intensity signal and a more clear punctate pattern (green colour), which was tentatively assigned to the lysosomes. This hypothesis was confirmed by a colocalization assay using the lysosomal marker LysoTracker DND-99 (red colour in Fig. 4). Merging the images for the emissions of **1–4** and Lysotracker DND-99 gives a better matching (yellow colour) for **3** (Pearson's correlation coefficient of 0.88; Fig. S8) than for **1**, **2** and **4** (Pearson's correlation coefficients 0.63, 0.53 and 0.56, respectively, Fig. S8).

To expand the scope of application of the studied cellular probes, and considering the excellent lysosomal accumulation of 3, its distribution was studied in another cell line, the adrenal carcinoma cell line SW13. In particular, SW13/cl.2 cells lack the cytoplasmic intermediate filament vimentin, which impairs the perinuclear distribution of lysosomes leading to their preferential localization at one side of the nucleus [44, 45]. Cultures of SW13/cl.2 cells were incubated with **1** or **3**. In this cell type, **1** did not generate a specific lysosome staining (Fig. 5, upper panels). Some vesicles without the typical appearance of lysosomes, i.e., larger than expected (see enlarged image at the right) stand out in some cells on a non-negligible, mainly cytoplasmic background, in which other apparently membranous structures can be seen. In contrast, **3** yielded a more typical pattern with small vesicles accumulated at one side of the nucleus (Fig. 5, lower panels). In cells of patients affected by Niemann Pick C disease the lysosomes are abnormally enlarged due to the accumulation of cholesterol [7]. A correct visualization of this defective process is fundamental to carry out reliable metabolic studies, and thus we used this context to validate the superior ability of **3** over **1** to obtain images of the lysosomes with enough quality. Hence, cultures of SW13/cl.2 human adrenal carcinoma cells were treated with the inhibitor of lysosomal cholesterol export U18666A, which leads to the enlargement of the lysosomes due to the accumulation of the aforementioned lipid [34] and incubated with **1** or **3**. This approach has been used in the past to create valid pharmacological models of the Niemann-Pick C disease [45,46]. As it can be seen in Fig. 5, in cells treated with U18666A and incubated with **1**, a non-specific staining pattern was obtained, with a moderate increase in the intensity of the juxtanuclear structures, but persistence of the cytoplasmic background. In contrast, **3** reveals the typical clustering of lysosomes into larger and better-defined vesicles in a juxtanuclear distribution, indicating that the distribution of this probe reflects the alterations in lysosomal dynamics.

Additionally, we were interested in assessing the behaviour of these fluorescent molecules after fixation. In control fixed cells (Fig. 6), the signals from both **1** and **3** displayed a non-specific pattern with some background and scattered vesicular staining. Only U18666A-treated cells stained with **3** retained an apparently specific staining of juxtanuclear lysosome accumulations. Thus, live cell visualization of **3** appears to be superior, and further optimization would be required for the preservation of the fluorescent signal.

The high contrast obtained by **3** makes this compound potentially useful in combination with other probes marking specific molecules inside the lysosome, like filipin, which is able to stain deposits of cholesterol in Niemann-Pick C cells [47,48]. It remains to be determined whether **3** stains any particular biomolecule within the organelle or just accumulates in this acidic organelle in response to protonation. This latter mechanism of internalisation is the most likely occurring since the dialkylamino substitution is found in many fluorescent probes [13,15, 16,49,50] and numerous lysosomotropic drugs increasing the pH of the lysosome [51,52].
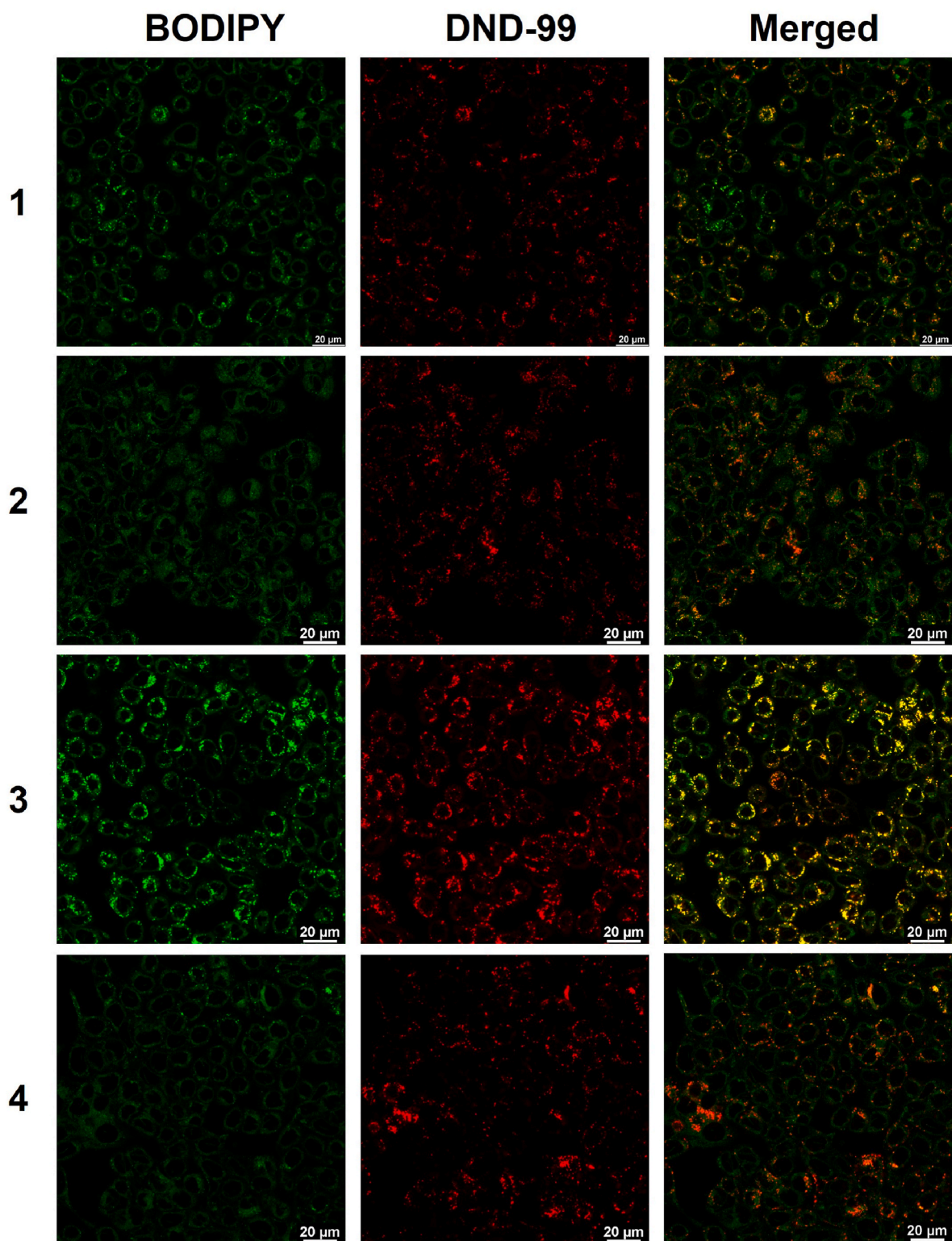
Fig. 4. Colocalization of **1–4** with LysoTracker DND-99 in HT-29 cells. HT-29 cells were preincubated with **1–4** (10 nM) for 20 min, followed by incubation with LysoTracker DND-99 (100 nM) for 30 min. Bars, 20 μm.

4. Conclusion

In summary, a series of four BODIPY derivatives made with amino acid building blocks have been synthesized and characterized (NMR techniques, mass spectrometry and UV–Vis/fluorescence spectroscopies). In 0.1 M HEPES, pH 7.00, at a concentration of 10 μM, three of the compounds (**1**, **2** and **4**) form weakly emissive nanoparticles (DLS

studies) whereas one of them (**3**), containing lysine as a building block, remains solubilized being highly fluorescent. The tendency to aggregation is also important for **3** at high concentration (100 μM), whereas at 10 nM this phenomenon is absent for all the compounds. The cellular uptake of **1–4** has been studied in human colon adenocarcinoma cells HT-29 by means of flow cytometry and confocal laser scanning microscopy. All the compounds were efficiently internalized, but with a
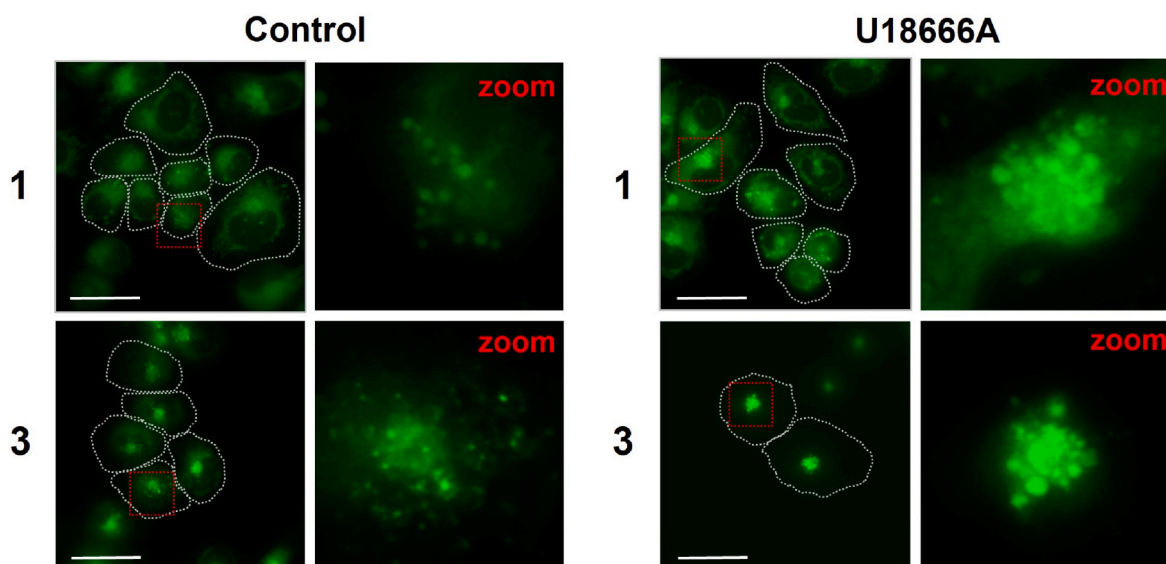
Fig. 5. Fluorescent signals generated by **1** and **3** in SW13/cl.2 cells. Cells were treated with vehicle (control) or U18666A, and subsequently incubated with **1** or **3**, as indicated. Fluorescence was monitored in live cells. The cell contour is marked by dotted lines. The square regions of interest are enlarged in the panels at the right (zoom). Bars, 40 μm.
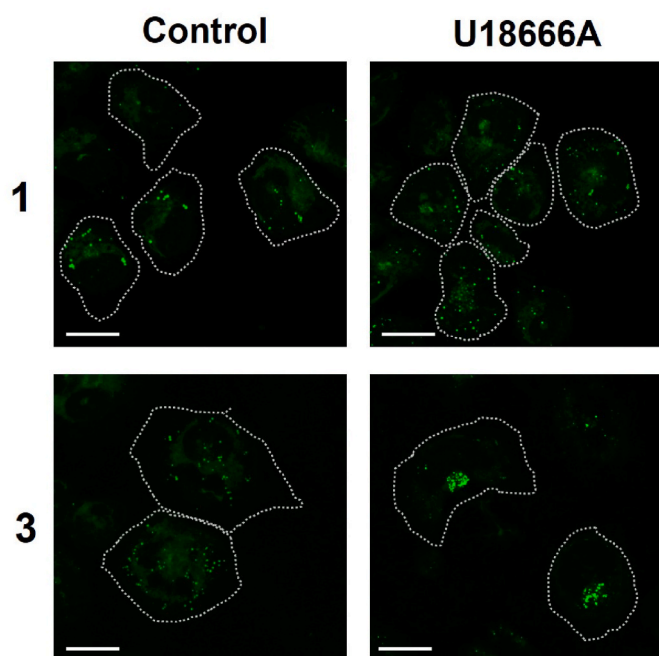

Fig. 6. Detection of **1** and **3** after cell fixation. SW13/cl.2 cells were treated and incubated with molecules **1** or **3** as described in Fig. 5. Subsequently, cells were fixed with 4% (w/v) paraformaldehyde and fluorescent signals detected by confocal microscopy. Bars, 20 μm.

notable preference by molecule **3**. The lysosomal location of all the molecules has been demonstrated by means of colocalization assays using lysosomal fluorescent probe LysoTracker DND-99. In this regard, the soluble compound **3** was the one showing a more specific lysosomal location (Pearson's correlation coefficient 0.88). Molecules **3** and **1** were also tested in a cellular model of lysosomal storage disease (SW13/cl.2 human adrenal carcinoma). In this case, **3** showed a clear better performance in fluorescence microscopy assays, marking the lysosomes of cells treated with the inhibitor of lysosomal cholesterol export U18666A with a higher definition than **1**. We hope that these studies will shed light on the structural factors causing the aggregation of these

derivatives and the influence of such self-assembly process on the microscopic imaging of lysosomal vesicles.

Author contribution statement

FG and JFM designed and supervised the study. DNV and CAAP synthesized the molecules under study. DNV and BB performed the flow citometry experiments and part of the miscroscopy studies. DPS performed part of the miscroscopy studies (Niemann-Pick C). DPS, JFM and FG wrote parts of the manuscript. DNV edited the manuscript. All authors read and approved the final version.

Declaration of Competing Interest

The authors declare that they have no known competing financial interests or personal relationships that could have appeared to influence the work reported in this paper.

Acknowledgements

The authors acknowledge the financial support from the Spanish Ministry of Science and Innovation co-funded by the European Regional Development Fund of the European Union (grant RTI2018-096748-B-I00 to FG and RTI2018-097624-B-I00 to DPS). Technical support by SCIC-UJI is acknowledged.

Appendix A. Supplementary data

Supplementary data to this article can be found online at https://doi.org/10.1016/j.dyepig.2022.110236.

References

[1] Lawrence RE, Zoncu R. The lysosome as a cellular centre for signalling, metabolism and quality control. Nat Cell Biol 2019;21:133–42. https://doi.org/10.1038/s41556-018-0244-7.
[2] Ma Z, Li J, Lin K, Ramachandran M, Zhang D, Showalter M, et al. Pharmacophore hybridisation and nanoscale assembly to discover self-delivering lysosomotropic new-chemical entities for cancer therapy. Nat Commun 2020;11:4615. https://doi.org/10.1038/s41467-020-18399-4.
[3] Whyte LS, Lau AA, Hemsley KM, Hopwood JJ, Sargeant TJ. Endo-lysosomal and autophagic dysfunction: a driving factor in Alzheimer's disease? J Neurochem 2017;140:703–17. https://doi.org/10.1111/jnc.13935.

[4] Savarino A, Boelaert JR, Cassone A, Majori G, Cauda R. Effects of chloroquine on viral infections: an old drug against today's diseases? Lancet Infect Dis 2003;3: 722–7. https://doi.org/10.1016/S1473-3099(03)00806-5.

[5] Khan N, Chen X, Geiger JD. Role of endolysosomes in severe acute respiratory syndrome coronavirus-2 infection and coronavirus disease 2019 pathogenesis: implications for potential treatments. Front Pharmacol 2020;11:595888. https://doi.org/10.3389/fphar.2020.595888.

[6] Fukuda T, Ewan L, Bauer M, Mattaliano RJ, Zaal K, Ralston E, et al. Dysfunction of endocytic and autophagic pathways in a lysosomal storage disease. Ann Neurol 2006;59:700–8. https://doi.org/10.1002/ana.20807.

[7] Parenti G, Medina DL, Ballabio A. The rapidly evolving view of lysosomal storage diseases. EMBO Mol Med 2021;13:e12836. https://doi.org/10.15252/emmm.202012836.

[8] Vanier MT. Niemann-Pick disease type C. Orphanet J Rare Dis 2010;5:16.

[9] Zhu H, Fan J, Xu Q, Li H, Wang J, Gao P, et al. Imaging of lysosomal pH changes with a fluorescent sensor containing a novel lysosome-locating group. Chem Commun 2012;48:11766–8. https://doi.org/10.1039/c2cc36785h.

[10] Lv HS, Huang SY, Xu Y, Dai X, Miao JY, Zhao BX. A new fluorescent pH probe for imaging lysosomes in living cells. Bioorg Med Chem Lett 2014;24:535–8. https://doi.org/10.1016/j.bmcl.2013.12.025.

[11] Ying LQ, Branchaud BP. Selective labeling and monitoring pH changes of lysosomes in living cells with fluorogenic pH sensors. Bioorg Med Chem Lett 2011; 21:3546–9. https://doi.org/10.1016/j.bmcl.2011.04.137.

[12] Loudet A, Ueno Y, Wu L, Jose J, Barhoumi R, Burghardt R, et al. Organelle-selective energy transfer: a fluorescent indicator of intracellular environment. Bioorg Med Chem Lett 2011;21:1849–51. https://doi.org/10.1016/j.bmcl.2011.01.040.

[13] Zheng X, Zhu W, Ni F, Ai H, Gong S, Zhou X, et al. Simultaneous dual-colour tracking lipid droplets and lysosomes dynamics using a fluorescent probe. Chem Sci 2019;10:2342–8. https://doi.org/10.1039/C8SC04462G.

[14] Rong RX, Wang SS, Liu X, Li RF, Wang KR, Cao ZR, et al. Lysosomes-targeting imaging and anticancer properties of novel bis-naphthalimide derivatives. Bioorg Med Chem Lett 2018;28:742–7. https://doi.org/10.1016/j.bmcl.2018.01.008.

[15] Kim HM, An MJ, Hong JH, Jeong BH, Kwon O, Hyon JY, et al. Two-photon fluorescent probes for acidic vesicles in live cells and tissue. Angew Chem Int Ed 2008;47:2231–4. https://doi.org/10.1002/anie.200704586.

[16] Lim CS, Hong ST, Ryu SS, Kang DE, Cho BR. Two-photon probes for lysosomes and mitochondria: simultaneous detection of lysosomes and mitochondria in live tissues by dual-color two-photon microscopy imaging. Chem Asian J 2015;10: 2240–9. https://doi.org/10.1002/asia.201500314.

[17] Zacharioudakis E, Cañeque T, Custodio R, Müller S, Cuadro AM, Vaquero JJ, et al. Quinolizinium as a new fluorescent lysosomotropic probe. Bioorg Med Chem Lett 2017;27:203–7. https://doi.org/10.1016/j.bmcl.2016.11.074.

[18] Zhou X, Fang Y, Lesiak L, Stains CI. A phosphinate-containing fluorophore capable of selectively inducing apoptosis in cancer cells. Chembiochem 2019;20:1712–6. https://doi.org/10.1002/cbic.201800811.

[19] Galindo F, Burguete MI, Vigara L, Luis SV, Kabir N, Gavrilovic J, et al. Synthetic macrocyclic peptidomimetics as tunable pH probes for the fluorescence imaging of acidic organelles in live cells. Angew Chem Int Ed 2005;44:6504–8. https://doi.org/10.1002/anie.200501920.

[20] Burguete MI, Galindo F, Izquierdo MA, O'Connor JE, Herrera G, Luis SV, et al. Synthesis and evaluation of pseudopeptidic fluorescence pH probes for acidic cellular organelles: in vivo monitoring of bacterial phagocytosis by multiparametric flow cytometry. Eur J Org Chem 2010. https://doi.org/10.1002/ejoc.201000854. 5967–79.

[21] Marín MJ, Galindo F, Thomas P, Russell DA. Localized intracellular pH measurement using a ratiometric photoinduced electron-transfer-based nanosensor. Angew Chem Int Ed 2012;51:9657–61. https://doi.org/10.1002/anie.201203866.

[22] Wadhavane PD, Izquierdo MÁ, Lutters D, Burguete MI, Marín MJ, Russell DA, et al. Fluorescent macrocyclic probes with pendant functional groups as markers of acidic organelles within live cells. Org Biomol Chem 2014;12:823–31. https://doi.org/10.1039/c3ob41773e.

[23] Saura AV, Marín MJ, Burguete MI, Russell DA, Galindo F, Luis SV. The synthesis of new fluorescent bichromophoric compounds as ratiometric pH probes for intracellular measurements. Org Biomol Chem 2015;13:7736–49. https://doi.org/10.1039/c5ob00704f.

[24] Vanessa Saura A, Isabel Burguete M, Galindo F, Luis SV. Novel fluorescent anthracene-bodipy dyads displaying sensitivity to pH and turn-on behaviour towards Cu(II) ions. Org Biomol Chem 2017;15:3013–24. https://doi.org/10.1039/C7OB00274B.

[25] Izquierdo MA, Wadhavane PD, Vigara L, Burguete MI, Galindo F, Luis SV. The interaction of amino acids with macrocyclic pH probes of pseudopeptidic nature. Photochem Photobiol Sci 2017;16:1320–6. https://doi.org/10.1039/c7pp00167c.

[26] Xu W, Zeng Z, Jiang JH, Chang YT, Yuan L. Discerning the chemistry in individual organelles with small-molecule fluorescent probes. Angew Chem Int Ed 2016;55: 13658–99. https://doi.org/10.1002/anie.201510721.

[27] Gao P, Pan W, Li N, Tang B. Fluorescent probes for organelle-targeted bioactive species imaging. Chem Sci 2019;10:6035–71. https://doi.org/10.1039/c9sc01652j.

[28] Urano Y, Asanuma D, Hama Y, Koyama Y, Kamiya M, Nagano T, et al. Selective molecular imaging of viable cancer cells with pH-activatable fluorescence probes. Nat Med 2009;15:104–9. https://doi.org/10.1038/nm.1854.Selective.

[29] Trapp S, Rosania GR, Horobin RW, Kornhuber J. Quantitative modeling of selective lysosomal targeting for drug design. Eur Biophys J 2008;37:1317–28. https://doi.org/10.1007/s00249-008-0338-4.

[30] Horobin RW, Stockert JC, Rashid-Doubell F. Uptake and localisation of small-molecule fluorescent probes in living cells: a critical appraisal of QSAR models and a case study concerning probes for DNA and RNA. Histochem Cell Biol 2013;139: 623–37. https://doi.org/10.1007/s00418-013-1090-0.

[31] Yang H, Li X, Cai Y, Wang Q, Li W, Liu G, et al. Silico prediction of chemical subcellular localization via multi-classification methods. Medchemcomm 2017;8: 1225–34. https://doi.org/10.1039/c7md00074j.

[32] Sarria AJ, Lieber JG, Nordeen SK, Evans RM. The presence or absence of a vimentin-type intermediate filament network affects the shape of the nucleus in human SW-13 cells. J Cell Sci 1994;107:1593–607. https://doi.org/10.1242/jcs.107.6.1593.

[33] Duarte S, Viedma-Poyatos Á, Navarro-Carrasco E, Martínez AE, Pajares MA, Pérez-Sala D. Vimentin filaments interact with the actin cortex in mitosis allowing normal cell division. Nat Commun 2019;10:1–19. https://doi.org/10.1038/s41467-019-12029-4.

[34] Lu F, Liang Q, Abi-Mosleh L, Das A, de Brabander JK, Goldstein JL, et al. Identification of NPC1 as the target of U18666A, an inhibitor of lysosomal cholesterol export and Ebola infection. Elife 2015;4:e12177. https://doi.org/10.7554/eLife.12177.

[35] Oeste CL, Pinar M, Schink KO, Martínez-Turrión J, Stenmark H, Penalva MA, et al. An isoprenylation and palmitoylation motif promotes intraluminal vesicle delivery of proteins in cells from distant species. PLoS One 2014;9:e107190. https://doi.org/10.1371/journal.pone.0107190.

[36] Navarro-Barreda D, Angulo-Pachón CA, Bedrina B, Galindo F, Miravet JF. A dual stimuli responsive supramolecular gel provides insulin hydrolysis protection and redox-controlled release of actives. Macromol Chem Phys 2020;221:1–6. https://doi.org/10.1002/macp.201900419.

[37] Navarro-Barreda D, Angulo-Pachón CA, Galindo F, Miravet JF. Photoreversible formation of nanotubes in water from an amphiphilic azobenzene derivative. Chem Commun 2021;57:11545–8. https://doi.org/10.1039/d1cc04319f.

[38] Navarro-Barreda D, Bedrina B, Galindo F, Miravet JF. Glutathione-responsive molecular nanoparticles from a dianionic bolaamphiphile and their use as carriers for targeted delivery. J Colloid Interface Sci 2022;608. https://doi.org/10.1016/j.jcis.2021.10.142. 2009–17.

[39] Loudet A, Burgess K. BODIPY dyes and their derivatives: syntheses and spectroscopic properties. Chem Rev 2007;107:4891–932. https://doi.org/10.1021/cr078381n.

[40] Radunz S, Tschiche HR, Moldenhauer D, Resch-Genger U. Broad range ON/OFF pH sensors based on pKa tunable fluorescent BODIPYs. Sensor Actuator B Chem 2017; 251:490–4. https://doi.org/10.1016/j.snb.2017.05.080.

[41] Radunz S, Kraus W, Bischoff FA, Emmerling F, Tschiche HR, Resch-Genger U. Temperature- and structure-dependent optical properties and photophysics of BODIPY dyes. J Phys Chem 2020;124:1787–97. https://doi.org/10.1021/acs.jpca.9b11859.

[42] Bergström F, Mikhalyov I, Hägglöf P, Wortmann R, Ny T, Johansson LB. Dimers of dipyrrometheneboron difluoride (BODIPY) with light spectroscopic applications in chemistry and biology. J Am Chem Soc 2002;124:196–204. https://doi.org/10.1021/ja010983f.

[43] Mikhalyov I, Gretskaya N, Bergström F, Johansson LB. Electronic ground and excited state properties of dipyrrometheneboron difluoride (BODIPY): dimers with application to biosciences. Phys Chem Chem Phys 2002;4:5663–70. https://doi.org/10.1039/b206357m.

[44] Pérez-Sala D, Oeste CL, Martínez AE, Carrasco MJ, Garzón B, Cañada FJ. Vimentin filament organization and stress sensing depend on its single cysteine residue and zinc binding. Nature Communications 2015;6:7287. https://doi.org/10.1038/ncomms8287.

[45] Styers ML, Salazar G, Love R, Peden AA, Kowalczyk AP, Faundez V, et al. The endo-lysosomal sorting machinery interacts with the intermediate filament cytoskeleton. Mol Biol Cell 2004;15:5369–82. https://doi.org/10.1091/mbc.E04-03-0272.

[46] Pérez-Sala D, Boya P, Ramos I, Herrera M, Stamatakis K. The C-terminal sequence of RhoB directs protein degradation through an endo-lysosomal pathway. PLoS One 2009;4:e8117. https://doi.org/10.1371/journal.pone.0008117.

[47] Pipalia NH, Huang A, Ralph H, Rujoi M, Maxfield FR. Automated microscopy screening for compounds that partially revert cholesterol accumulation in Niemann-Pick C cells. J Lipid Res 2006;47:284–301. https://doi.org/10.1194/jlr.M500388-JLR200.

[48] Sitarska D, Ługowska A. Laboratory diagnosis of the Niemann-Pick type C disease: an inherited neurodegenerative disorder of cholesterol metabolism. Metab Brain Dis 2019;34:1253–60. https://doi.org/10.1007/s11011-019-00445-w.

[49] Zhao X, Wang C, Yuan G, Ding H, Zhou L, Liu X, et al. A dual-site modulated FRET-based two-photon ratiometric fluorescent probe for tracking lysosomal pH changes in living cells, tissues and zebrafish. Sensor Actuator B Chem 2019;290:79–86. https://doi.org/10.1016/j.snb.2019.03.122.

[50] Sun SG, Ding H, Yuan G, Zhou L. An efficient TP-FRET-based lysosome-targetable fluorescent probe for imaging peroxynitrite with two well-resolved emission channels in living cells, tissues and zebrafish. Anal Chim Acta 2020;1100:200–7. https://doi.org/10.1016/j.aca.2019.11.065.

[51] Villamil Giraldo AM, Appelqvist H, Ederth T, Öllinger K. Lysosomotropic agents: impact on lysosomal membrane permeabilization and cell death. Biochem Soc Trans 2014;42:1460–4. https://doi.org/10.1042/BST20140145.

[52] Norinder U, Tuck A, Norgren K, Munic Kos V. Existing highly accumulating lysosomotropic drugs with potential for repurposing to target COVID-19. Biomed Pharmacother 2020;130:110582. https://doi.org/10.1016/j.biopha.2020.110582.